Steel and Composite Structures, *Vol. 59, No. 5 (2026) 609-629*
https://doi.org/10.12989/scs.2026.59.5.609

Techno-Press

Coupled effects of corrosion and fault-crossing ground motions on continuous rigid frame bridges: Nonlinear dynamic response and failure mechanisms

Hongyu Jia*[1,2], Jiahao Hou[2a], Hao Bai[3b], Zhi Xu[4c], Kang Jia[5d], Shixiong Zheng[1,2e]

[1]State Key Laboratory of Bridge Intelligent and Green Construction, Southwest Jiaotong University, Chengdu, 611756, Sichuan, China
[2]School of Civil Engineering, Southwest Jiaotong University, Chengdu, 610031, China
[3]Sichuan Expressway Construction & Development Group Co., Ltd., Chengdu, 610041, China
[4]Shudao Investment Group Co., Ltd., Chengdu, 610094, China
[5]Sichuan Chengdu Construction Engineering Group Co., Ltd., Chengdu 610000, Sichuan, China

(Received February 4, 2026, Revised April 9, 2026, Accepted May 1, 2026)

Abstract. Bridges traversing active faults in aggressive environments (such as coastal or reservoir regions) face the coupled risks of chloride-induced corrosion and fault-crossing seismic excitations. The failure mechanisms governing continuous rigid frame bridges (CRFBs) under such coupled degradation-seismic conditions remain poorly understood. This study develops an integrated analytical framework comprising: (i) time-dependent deterioration models accounting for chloride-induced reinforcement section loss, yield-strength reduction, and concrete cover softening; and (ii) a refined 3D nonlinear finite element model (FEM) incorporating fiber beam-column elements, a soil-structure interaction system (SSIS), bearings, and pounding effects. (iii) Synthetic fault-crossing ground motions are generated by superimposing low-frequency fling-step pulses onto spectrum-matched high-frequency records. These synthetic motions are then applied to the bridge model via multi-support excitation. Comparative analyses demonstrate that fault-crossing motions shift the structural response from an inertia-dominated amplification mode to a quasi-static forced displacement mode. This mode shift imposes significantly larger and more asymmetric kinematic demands compared to standard near-fault scenarios. Structural responses exhibit a nonlinear dependence on permanent ground rupture displacement (PGRD), typically plateauing at an observed peak of 0. 6 m for the examined cases. This phenomenon is attributed to a force-limiting mechanism: the yielding of foundation soil and the premature plastic hinging of corroded piers restrict the inertial force transmission to the superstructure. Furthermore, the fault-crossing angle (FCA) governs the demand distribution, exhibiting an 'M-shaped' sensitivity; deviation from orthogonality amplifies pier-base curvature by up to three orders of magnitude due to longitudinal locking effects. A frequency-decoupling mechanism is also identified: low-frequency pulses dictate global pier drifts and permanent bearing offsets, whereas high-frequency components control local cyclic damage. Crucially, corrosion accelerates pier yielding and exacerbates the accumulation of plastic damage, thereby substantially amplifying the collapse probability under the extreme forced displacements induced by fault rupture.

*Corresponding author, Ph. D., Associate Professor, E-mail: hongyu1016@swjtu.edu.cn
[a] M.S. Student, E-mail: houjiahao@my.swjtu.edu.cn
[b] Professor, E-mail: secdcbh@126.com
[c] Ph.D. Student, E-mail: xuzhi2021@my.swjtu.edu.cn
[d] M.S., E-mail: jk1122@my.swjtu.edu.cn
[e] Professor, E-mail: zhengsx@home.swjtu.edu.cn

http://www.techno-press.org/scs/5

ISSN: 1229-9367 (Print), 1598-6233 (Online)

Keywords: continuous rigid frame bridge; corrosion-induced degradation; fault-crossing ground motion; frequency decoupling; soil-structure interaction system

1. Introduction

Large-scale transportation infrastructure serves as a strategic lifeline for regional economic integration. However, due to rigorous alignment constraints in complex geological environments, long-span bridges are frequently compelled to traverse active fault rupture zones. During surface faulting episodes, bridges straddling the fracture zone are subjected to a superposition of PGRD and severe high-velocity impulsive motions [1-7]. This combination of quasi-static forced deformations and inertial dynamic loads induces structural behaviors that diverge radically from those observed under typical far-field excitations [8-13]. Despite the critical function of such infrastructure, the interaction mechanisms between corrosion-induced stiffness degradation and the extreme demands of fault-crossing seismicity are poorly understood.

Fault-crossing bridges are frequently situated in aggressive environments (coastal or reservoir areas) where exposure to chloride significantly accelerates material deterioration [14-19]. Unlike seismic excitations, which are random across spatial and temporal scales, corrosion damage propagates as a cumulative, time-dependent process; consequently, the safety margins against collapse are continuously eroding. A critical engineering challenge is to quantify whether the residual capacity of the corroded system remains sufficient to accommodate the extreme seismic demands imposed by a fault rupture event.

Extensive investigations have been conducted on the dynamic response of various bridge typologies subjected to fault-crossing excitations. Lin et al. [20, 21] analyzed simply supported bridges and identified that low-frequency velocity pulses dictate the collapse mechanisms. Similarly, Hu et al. [22] investigated a three-span cable-stayed bridge, revealing that the PGRD governs the kinematic response of the girder and bearings. Regarding the FCA, Zeng et al. [23] reported that an orthogonal crossing configuration minimizes structural demands and mitigates biaxial pylon nonlinearity. Jia et al. [24] further highlighted the geometric sensitivity of suspension bridges, noting that acute crossing angles significantly amplify the risk of girder unseating. However, these studies generally assume a time-invariant structural capacity. This simplification neglects the material degradation caused by environmental corrosion, which progressively reduces the bridge's resistance to the imposed fault displacements throughout its service life.

The coupled impact of corrosion-induced deterioration and seismic excitation has received increasing attention. Herrera and Tolentino [25] quantified that structural failure probability is significantly amplified under combined corrosion-seismic scenarios compared to seismic loading alone. At the component level, Ni Choine et al. [26] utilized a cyclic buckling constitutive model to demonstrate that pitting corrosion degrades fatigue life and buckling capacity more severely than uniform corrosion. Cui et al. [27] further identified the nonlinear temporal evolution of damage probability, though their study did not fully account for the shear-critical behavior induced by hoop reinforcement corrosion. Addressing this limitation, Xu et al. [28] developed a numerical framework for flexural-shear interaction, revealing that hoop reinforcement corrosion triggers a brittle shear failure mechanism in bridge piers. Li et al. [29] incorporated uncertainties in corrosion and near-fault spatial variability, confirming that ground motion variability further escalates damage probability. However, existing studies remain focused on conventional or near-fault ground motions. The coupled effects of corrosion-induced stiffness and strength degradation under the extreme kinematic demands of fault rupture remain inadequately explored. Therefore, a systematic investigation into these coupled degradation mechanisms and failure modes is essential for assessing the survivability of CRFBs straddling active faults.

Based on the above discussion, this study utilizes nonlinear dynamic response analysis to elucidate the damage evolution mechanisms of CRFBs. Specifically, the study quantifies the additional response amplification and incremental damage induced by corrosion, which are superimposed on the baseline demands of fault-crossing excitations. The framework of the study is as follows: Section 2 introduces the time-dependent material degradation model and the establishment of the refined nonlinear FEM. Section 3 details the synthesis of fault-crossing ground motions and the selection strategy based on spectral matching. Section 4 presents a comparative analysis of structural responses under near-fault versus fault-crossing scenarios to identify critical mechanism transitions. Section 5 investigates the sensitivity of the seismic response to key parameters: PGRD, FCA, and frequency content, and Section 6 summarizes the main conclusions.

2. Engineering background and numerical modeling

2.1 Description of the CRFB

As illustrated in Fig. 1(a), the prototype structure is a span arrangement of 125 + 220 + 125 m, flanked by two 50 m simply supported beam bridges (SSBBs). A single-cell box cross-section was adopted for the main girder. Regarding the substructure, the main piers (Piers 3 and 4) utilize rectangular hollow cross-sections to provide significant lateral stiffness, while the transition piers (Piers 2 and 5) are constructed with thin-walled hollow double-column sections. Concrete grades C40 and C60 were assigned to the piers and the main girder, respectively. Bi-directional sliding rubber bearings are installed at the top of the transition piers. Site Class is C according to the USGS classification. The bridge is designed in accordance with a seismic fortification intensity of VII.

2.2 Time-dependent material degradation models

The time-dependent material degradation is quantified through three governing parameters. The first is the reduction in the effective cross-sectional area of the reinforcement. For uniform corrosion scenarios (Fig. 1(b)), the residual cross-sectional area $A(t)$ is determined via Eq. (1), where i_{corr} denotes the corrosion rate, D_i represents the initial bar diameter, and T_i is the corrosion initiation time. Regarding localized pitting corrosion, the damage morphology is modeled as an idealized hemispherical void with a radius p (Fig. 1(c)), following established methodologies [30-32]. The consequent geometric reduction in the effective area is governed by Eq. (2), which p and b represent the pit depth and width, where $b = 2p\sqrt{1-(p/\phi)^2}$, $A_0 = \pi\phi^2/4$ denotes the pristine (uncorroded) bar. The geometric variables A_1 and A_2 are functions of the subtended angles θ_1 and θ_1, $A_1 = 0.5\left\{\theta_1\left(\frac{\phi}{2}\right)^2 - b\left|\frac{\phi}{2} - \frac{p^2}{\phi}\right|\right\}$, $A_2 = 0.5(\theta_2 p^2 - bp^2/\ \phi)$, $\theta_1 = 2\arcsin(b/\phi)$, $\theta_2 = 2\arcsin(0.5b/p)$. The second governing parameter is the reduction in

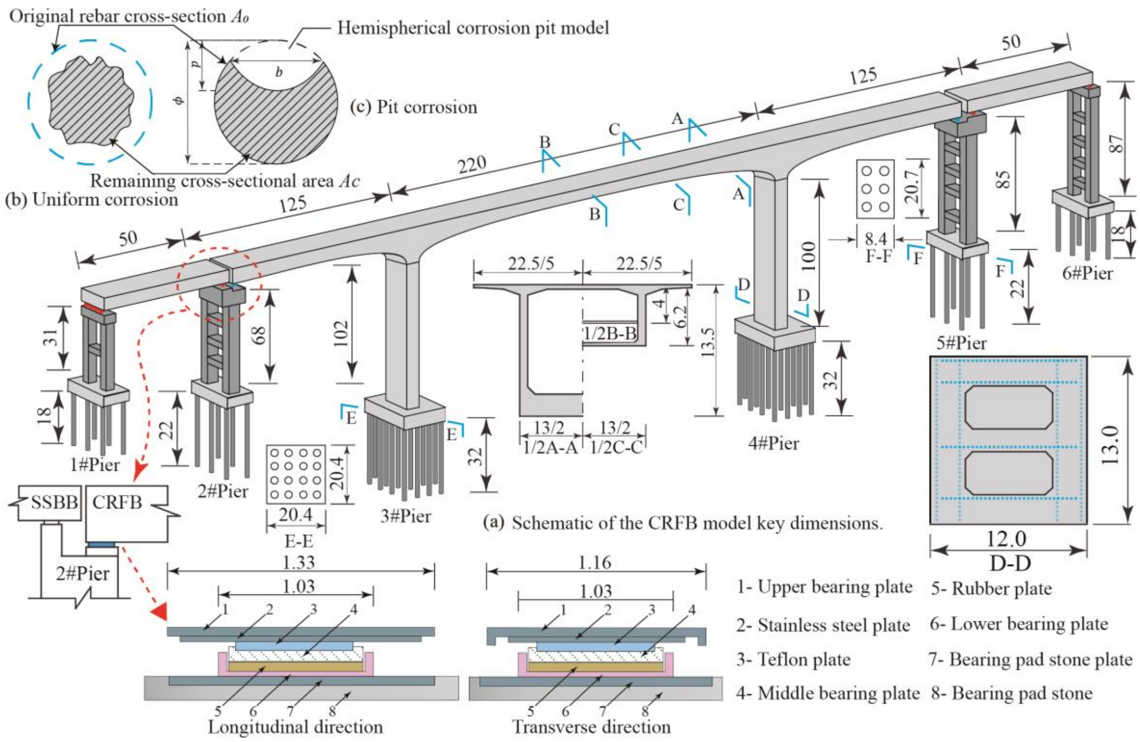

Figure 1. Schematic view of CRFBs and corrosion diagrams (Unit: m)

yield strength. During the corrosion process, the formation of pits induces stress concentrations and reduces the ductility of the steel. Consequently, the tensile yield capacity is compromised even in the remaining cross-section. To quantify this effect, the time-dependent constitutive model proposed by Du et al. [33] was adopted in Eq. (3), where Q_{corr} represents the mass loss ratio of the reinforcement, calculated via Eq. (4), d and d_s represent the nominal diameter of the uncorroded bar and the residual diameter after corrosion. Finally, the degradation of the concrete cover compressive strength is quantified. Due to the volumetric expansion of corrosion products, tensile cracks develop within the protective layer, softening its mechanical response. To simulate this effect, the strength reduction model proposed by Kashani et al. and Lin et al. [34, 35] was adopted, correlating the residual strength to the degree of corrosion expressed in Eq. (5). f_c and ε_c denote the peak compressive strength and corresponding strain of the intact unconfined concrete, while $f_{c0,corr}$ represents the degraded strength of the cover. ε_1 signifies the average tensile strain perpendicular to the compression direction. Geometric parameters include: n represents the number of longitudinal bars; v_{rs} is the volume expansion ratio of oxides, x_{cp} is corrosion penetration depth, b_0 is the section perimeter. It should be noted that the present numerical framework assumes a uniform corrosion profile along the height of the reinforced concrete piers. In authentic aggressive environments, chloride ingress and the ensuing material deterioration exhibit pronounced spatial variability. However, numerous seismic damage cases indicate that the main structural damage of continuous rigid frame bridges usually occurs at the bottom of the piers. Therefore, in this study, to simplify the calculation and explore the most unfavorable conditions, it is assumed that the core area of the plastic hinge has undergone uniform severe corrosion. This is relatively safer when exploring the limit of bearing capacity. Future research will further introduce a non-uniform corrosion model along the height of the pier to evaluate the precise impact of spatial variability on damage location. It is worth noting that while the current study adopts a deterministic approach for structural assessment, the modeling of reinforcement degradation has evolved to include more complex mechanisms. Recent studies have emphasized the importance of considering the non-uniformity of pitting corrosion through probabilistic frameworks [36, 37] and the critical role of stirrup-induced confinement loss in reducing the peak compressive strength of the concrete core [38].

$$A(t) = \begin{cases} D_i^2\pi & t < T_1 \\ D(t)^2\pi/4 & T_1 \\ 0 & 0.0203i_{corr} < t \end{cases} \tag{1}$$

$$A_{pit}(\theta_1,\theta_2) = \begin{cases} A_1 + A_2 & p \le \dfrac{\phi}{\sqrt{2}} \\ A_0 - A_1 + A_2 & \dfrac{\phi}{\sqrt{2}} < p \le \phi \\ A_0 & p \ge \phi \end{cases} \tag{2}$$

$$\begin{aligned} F &= (1.0 - 0.014Q_{corr})F_0 \\ \mathrm{f} &= (1.0 - 0.005Q_{corr})f_0 \end{aligned} \tag{3}$$

$$Q_{corr} = 1 - \left(\frac{d_s}{d}\right)^2 \tag{4}$$

$$f_{c0,corr} = \frac{f_{c0}}{1 + K\varepsilon_1/\varepsilon_{c0}}, \quad \varepsilon_1 = 2\pi n_{bars}(v_{rs} - 1)x_{cp}/b_0 \tag{5}$$

2.3 Establishment of three-dimensional refined nonlinear FEM

A refined three-dimensional nonlinear FEM was constructed using the OpenSEES framework [39]. To capture the dynamic coupling between the CRFB and the adjacent simply supported beam bridges (SSBBs), the model explicitly incorporates the nonlinear characteristics of girders, piers, bearings, and SSIS. The global finite element mesh and the constitutive schematics for these components are illustrated in Fig. 2.

Displacement-based beam-column elements with fiber sections were employed to simulate the elastoplastic behavior of piers and piles. To balance computational efficiency with simulation accuracy, a hybrid modeling strategy was adopted for the main girder. Nonlinear fiber elements were assigned to critical damage-prone regions [40, 41], including pier-girder connections, closure segments, and quarter-span sections, while the remaining segments were modeled elastically. Concrete behavior was modeled using the Concrete02 material (Fig. 2(e)), utilizing Mander's theoretical model [42] to define the confined and unconfined stress-strain relationships. Reinforcing steel was simulated using the Steel02 material, based on the Giuffré-Menegotto-Pinto model to capture isotropic strain hardening. It should be noted that while the corrosion-induced damage is macroscopically simulated by degrading the effective mechanical indicators (as defined in Eqs. (3)-(5)), the standard Steel02 material model cannot explicitly track localized inelastic buckling or low-cycle fatigue rupture. Consequently, the exclusion of such localized extreme fracture behaviors in the current fiber section analysis is explicitly acknowledged as a research limitation of the numerical modeling.

For the CRFB, pot bearings were simulated using flatSliderBearing elements (Fig. 2(a)). A compression-only constitutive relationship was assigned to the vertical degree of freedom to capture potential beam-bearing separation (uplift). The horizontal response follows a coupled bidirectional friction model with a circular yield surface. Adopted parameters are: friction

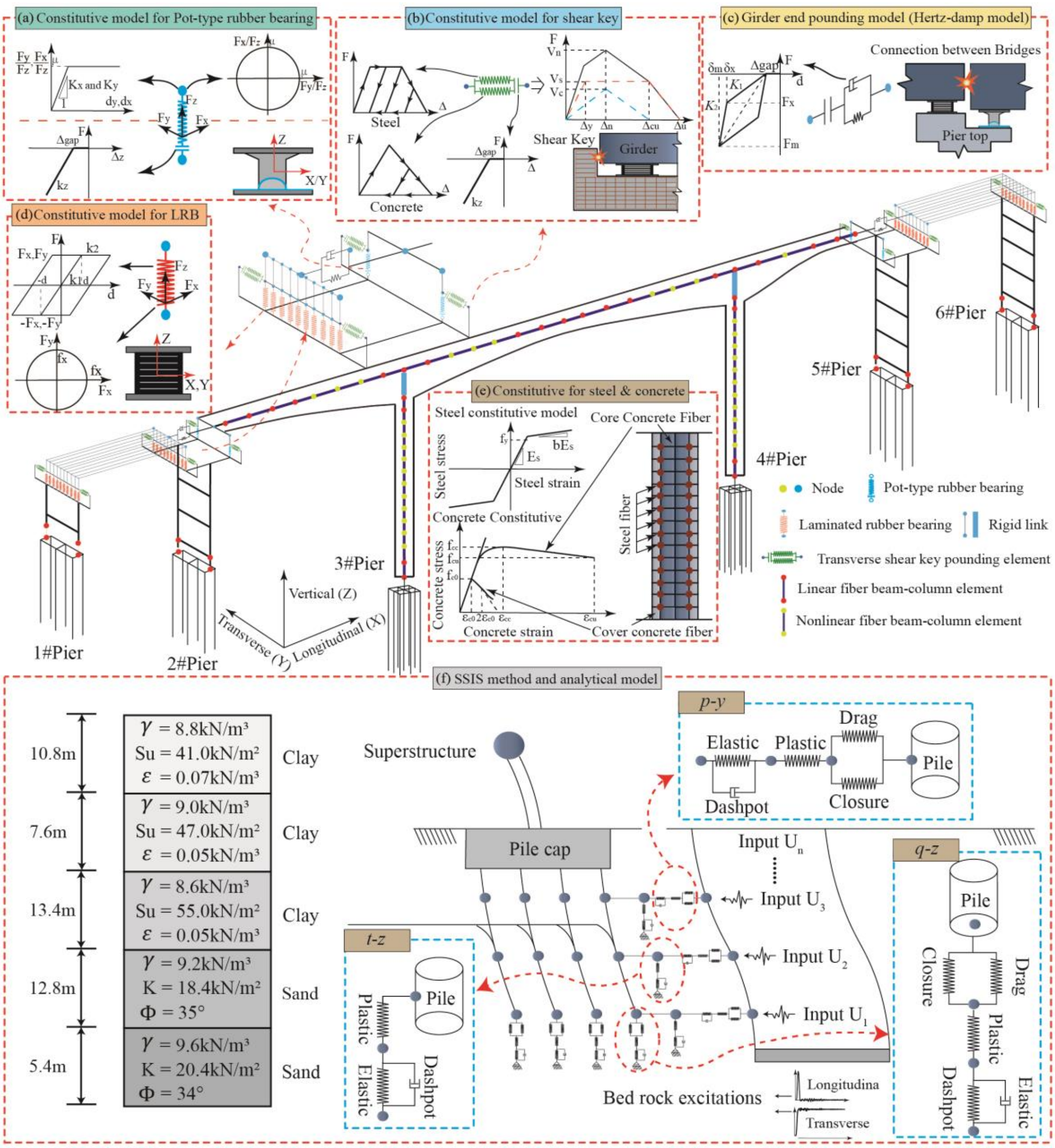

Figure 2. Three-dimensional nonlinear FEM (Unit: m)

coefficient $\mu = 0.02$, horizontal shear stiffness $K_x = K_y = 38000\ \mathrm{kN/m}$, vertical compressive stiffness $K_z = 1.07 \times 10^7\ \mathrm{kN/m}$, and the initial gap $\Delta_{gap} = 0$. Conversely, the laminated rubber bearings of the approach spans were modeled using elastomericBearingPlasticity elements (Fig. 2(d)). Key parameters include: initial elastic stiffness $k_1 = 1600\ \mathrm{kN/m}$, post-yield stiffness $k_2 = 0\ \mathrm{kN/m}$, and yield displacement $d_y = 0.002$ m.

Neglecting transverse constraints can underestimate seismic demands [43]. Thus, transverse shear keys were modeled using an elastic-plastic formulation, accounting for combined concrete and reinforcement contributions. As shown in Fig. 2(b), the inelastic behavior involves two parallel nonlinear springs in series with a gap element, implemented via the ElasticPPGap material [44]. Simultaneously, the Hertz-damp model was utilized to simulate longitudinal pounding between the girder ends (Fig. 2(c)). The constitutive parameters were calibrated as: initial stiffness $K_1 = 8580\ \mathrm{kN/mm}$, secondary stiffnesses $K_2 = 2900\ \mathrm{kN/mm}$, initial closing gap $\Delta_{gap} = 200$ mm, and yield displacement $\delta_x = 1.6$ mm.

Recognizing the critical role of foundation compliance in large-span bridges, a refined nonlinear SSIS model was established (Fig. 2(f)). The interaction mechanisms were simulated using zero-length nonlinear spring elements: p-y curves for lateral resistance, t-z curves for vertical skin friction, and q-z curves for pile-tip bearing. Mechanically, both p-y and q-z elements consist of a nonlinear spring arranged in series with a gap element (capturing soil detachment) and in parallel with a dashpot (representing radiation damping). Similarly, the t-z element integrates an elastic-plastic spring with a radiation damping dashpot to simulate skin friction degradation. The corrosion parameters for different time intervals are detailed in Table 1 based on the calculations in Section 2.2. The computed natural vibration periods of the uncorroded bridge exhibit strong agreement with results reported by Tong et al. [45, 46], as shown in Table 2, validating the accuracy of the established FEM.

Table 1. Values of corrosion model parameters at 0, 20, 40, 60, 80, and 100 years

Parameter	0 Years	20 Years	40 Years	60 Years	80 Years	100 Years
Rebar diameter (mm)	32.00	31.50	30.50	28.64	26.90	25.19
Rebar yield strength (MPa)	335.00	330.00	314.50	290.58	269.40	249.41
Concrete cover strength (MPa)	28.60	15.50	7.08	4.36	3.30	2.66

Table 2. Natural vibration periods of CRFBs at 0, 20, 40, 60, 80, and 100 years (Unit: s)

Mode	0 Years	20 Years	40 Years	60 Years	80 Years	100 Years
1	3.157	3.176	3.195	3.215	3.231	3.245
2	2.372	2.383	2.393	2.403	2.410	2.416
3	1.933	1.940	1.946	1.952	1.957	1.961
4	1.796	1.809	1.820	1.827	1.831	1.836
5	1.387	1.394	1.399	1.403	1.405	1.408
6	1.160	1.163	1.166	1.168	1.171	1.173
7	1.159	1.162	1.164	1.165	1.165	1.166
8	0.812	0.813	0.814	0.815	0.816	0.816
9	0.703	0.705	0.707	0.709	0.710	0.711
10	0.653	0.654	0.654	0.654	0.655	0.655

3. Synthesis and implementation of fault-crossing ground motions

Recorded fault-crossing ground motions are scarce in current databases. Therefore, a synthetic method was adopted to generate the input motions. This study superimposes a mathematical low-frequency (LF) pulse onto a processed high-frequency (HF) background record. Seed records were selected from the PEER database based on the design response spectrum (Table 3). Fig. 3 illustrates the response spectra of the selected suite. The mean spectrum exhibits a high degree of consistency with the target design spectrum.

To prevent spectral overlap with the synthetic pulse, a high-pass Butterworth filter (corner frequency = 0.1 Hz) was applied to these records. A cutoff frequency of 0.1 Hz (corresponding to a period of 10 s) was selected because the fundamental ductile period of the examined long-

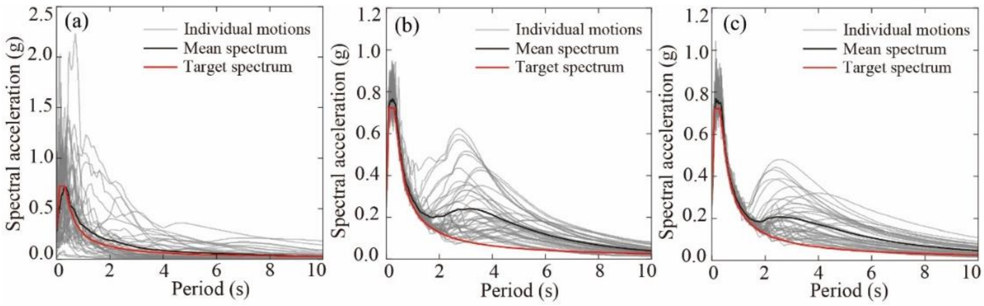

Figure 3. Near-fault and cross-fault seismic response spectrum curves: (a) is for near-fault, (b) is for the fault-parallel direction, (c) is for the fault-normal direction

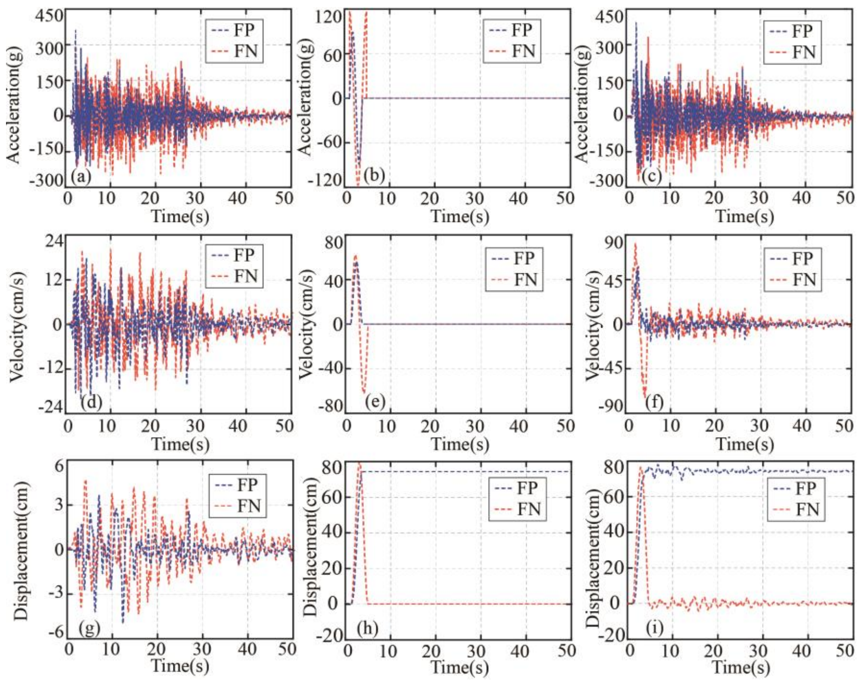

Figure 4. FP and FN fault-crossing ground motions based on the near-fault ground motion records

Table 3. Information on selected near-fault ground motion records

Event	RSN	Rjb/km	PGA (m/s^2)	PGV (cm/s)	PGD (cm)	PGV/PGA (s)
Northridge	1045	5.48	0.42	118.18	42.53	0.29
Northridge	982	5.43	0.41	111.47	44.64	0.28
Chi-Chi	1510	0.89	0.33	109.56	96.61	0.34
Imperial	159	0.65	0.19	41.68	11.60	0.22
Imperial	161	10.42	0.16	36.61	25.68	0.23
Imperial	170	7.31	0.24	73.39	48.00	0.32
Imperial	185	7.50	0.26	53.14	39.15	0.21
Imperial	171	0.07	0.32	72.95	34.92	0.23
Imperial	179	7.05	0.37	80.41	74.27	0.22
Imperial	181	1.35	0.45	113.55	72.89	0.26

span bridge, even under substantial inelastic deformations, remains generally below 10 s. This filtering strategy not only eliminates the potential interference from intrinsic baseline drifts in the original records but also reserves the requisite frequency band for the injection of long-period tectonic offsets. Given the highly non-stationary nature of fault-crossing ground motions, the long-period spectral ordinates of the synthesized records inevitably and reasonably exceed the conventional design spectrum. This spectral amplification physically reflects the unique destructive potential induced by massive permanent ground ruptures. This filter removes the original long-period components, retaining only the high-frequency transient vibrations, and the LF components were generated using analytical models to simulate two distinct near-fault effects. For the fault-parallel (FP) direction [47], the Abrahamson [48] model was used to simulate the permanent tectonic offset (Fling-step). The acceleration is defined as a single-cycle sine wave, which integrates into a monotonic displacement step; for the fault-normal (FN) direction, the Makris and Mavroeidis model [49-51] was used to simulate the velocity pulse caused by rupture propagation (Forward-Directivity). This model generates a large velocity pulse with zero residual displacement.

The final synthetic motions were obtained by summing the filtered HF records and the generated LF pulses. Fig. 4 presents the time histories of acceleration, velocity, and displacement for a representative synthetic motion. The fault-crossing ground motions are implemented using multi-support displacement excitation in the finite element analysis.

4. Comparison analysis of corroded CRFBs in near-fault and fault-crossing seismic

4.1 Dynamic responses of girder

While the response magnitudes vary, the fundamental seismic response trends and failure mechanisms remain consistent across the selected suite. Due to space constraints, two representative records were utilized for the detailed parametric study (closest to the mean spectral characteristics). Figs. 5 and 6 illustrate the envelope curves of the peak vertical and transverse displacements along the length of the main girder. These figures compare the bridge's response under near-fault versus fault-crossing scenarios for various corrosion durations. Under near-fault ground motions,

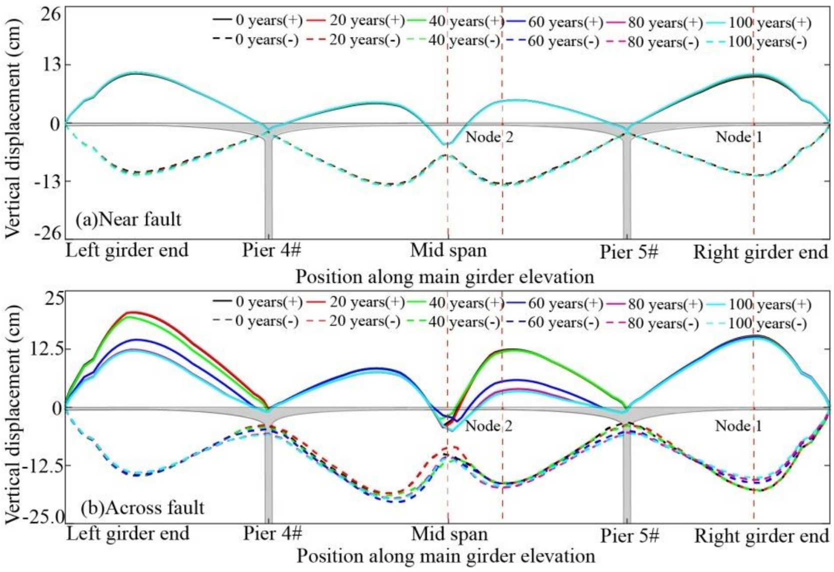

Figure 5. Envelope of vertical displacement of the main girder

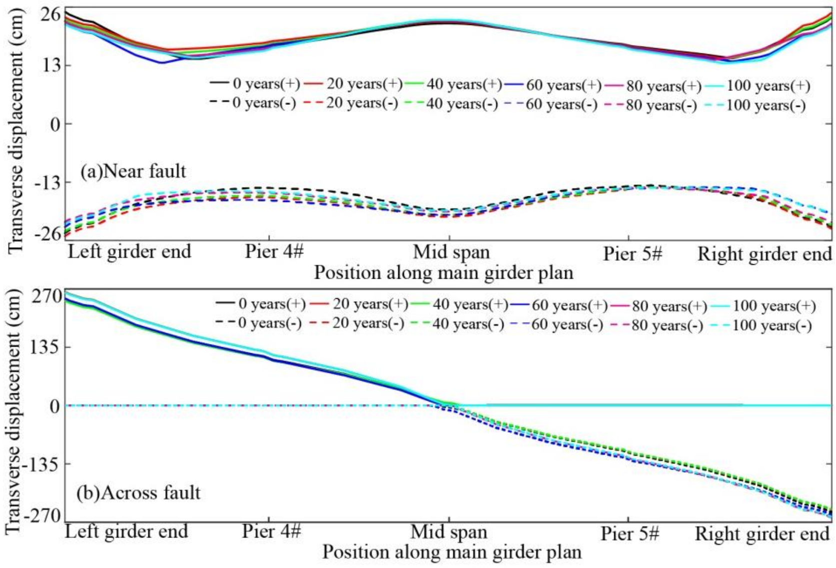

Figure 6. Envelope of transverse displacement of the main girder

corrosion causes only a minor increase in the girder's vertical displacement. The transverse displacement exhibits a symmetric oscillation about the initial equilibrium position, with peak amplitudes ranging from 13.5 cm to 24.8 cm. Conversely, under fault-crossing motions the vertical displacements are far greater than those in the near-fault case. The transverse displacement is dominated by the massive quasi-static ground offset, pushing the peak value to approximately 265 cm. Corrosion amplifies this response by reducing the overall structural stiffness. Furthermore, it should be noted that as the PGRD exceeds the aforementioned 0.6 m threshold, the massive relative displacement between the main girder and the approach spans rapidly exhausts the 200 mm initial gap, triggering severe longitudinal pounding. Notably, the corrosion-induced lateral stiffness degradation of the piers endows the main girder with greater longitudinal sliding freedom. From an engineering perspective, it is imperative to acknowledge that the calculated peak transverse displacement of approximately 265 cm significantly exceeds the physical stroke capacity of conventional pot bearings and the serviceability limits of expansion joints. In a real-world scenario, such extreme kinematic demands would inevitably result in the structural failure of the bearing system and potentially trigger the unseating of the main girder. While the current numerical model utilizes idealized constitutive relationships to quantify the maximum seismic demand imposed by the fault-crossing ground motions, the results highlight a catastrophic risk of unseating. Therefore, unseating prevention measures, such as the installation of high-capacity lateral seismic restrainers or cable restrainers, are critically essential for CRFBs straddling active fault zones to accommodate such massive quasi-static offsets.

4.2 Dynamic responses of pier

Fig. 7 displays the envelope curves of the maximum relative displacements in the longitudinal and transverse directions at pier 4 in different corrosion durations along the height of the pier. The pier's relative displacement increases with height. Furthermore, the displacements experienced under fault-crossing excitation are substantially larger than those under near-fault excitation [52]. The corrosion-induced increase in pier-top displacement can be as high as 11.5 cm under fault-crossing conditions; this indicates that the pier's response is more sensitive to corrosion under fault-crossing than under near-fault conditions. Fig. 8 presents the maximum moments and curvatures at the base of Pier 4 about the X and Y axes for various corrosion levels. The results show that the biaxial moments at the pier base are consistently larger in the fault-crossing case than in the near-fault case. Notably, the pier's response under fault-crossing excitation is more sensitive to corrosion, exhibiting greater changes in these base metrics. This heightened sensitivity leads to an amplification of curvature within the plastic hinge region, as illustrated in Fig. 9. Under near-fault excitation, curvature values generally confined within the range of $\pm 1.0 \times 10^{-4}\ \mathrm{m}^{-1}$, indicating that the pier primarily operates within the linear range with limited energy dissipation and minimal residual deformation. In contrast, fault-crossing scenarios induce extensive excursions into the nonlinear range and substantial residual drifts. The peak curvature reaches up to $-5.58 \times 10^{-4}\ \mathrm{m}^{-1}$, which is six times larger than near-fault case. The yielding plateaus evident

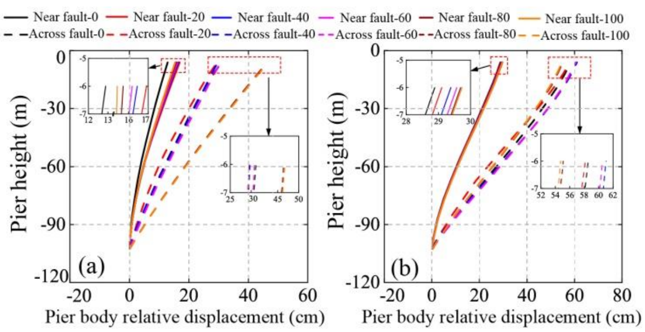

Figure 7. Maximum relative displacement along the height of pier 4: (a) The longitudinal directions; (b) The transverse directions

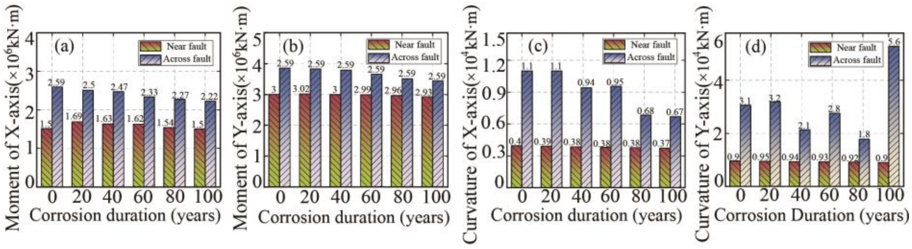

Figure 8. Maximum moment and curvature at the base of pier 4

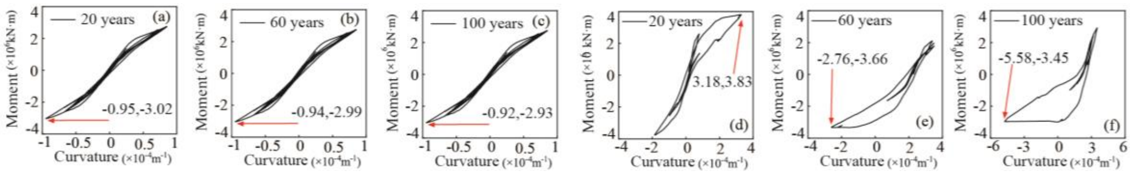

Figure 9. Moment-curvature curves at the base of pier 4: (a)-(c) near-fault ground motions, (d)-(f) fault-crossing ground motions

in the hysteresis loops unequivocally demonstrate that the pier has entered a significant elastic-plastic deformation state. Furthermore, as corrosion progresses from 20 to 100 years, the degradation of reinforcement and concrete confinement exacerbates the accumulation of plastic damage.

The response of girder and piers reveals a critical failure mechanism. Corrosion degrades the pier's capacity to resist imposed displacements, causing the pier to yield prematurely. This early yielding of the pier limits the inertial force transmitted to the main girder and consequently reduces the girder's upward displacement; however, it results in more severe localized damage in the pier and a larger downward displacement of the girder.

4.3 Dynamic responses of bearing

Fig. 10 shows the bearing displacement time-history for the bearing at pier 4. Under fault-crossing excitation, the bearing's displacements (both peak and residual) substantially exceed those in the near-fault case, and the peak bearing displacements under both near-fault and fault-crossing excitations exceed the maximum allowable displacement threshold of the pot bearings [53]. Moreover, the fault-crossing motion is characterized by a unidirectional pulse (due to fault rupture) and induces a distinct residual ~~offsets~~ in the transverse direction. The impact of corrosion on bearing demand is characterized by a non-monotonic trend. In the initial stages of degradation

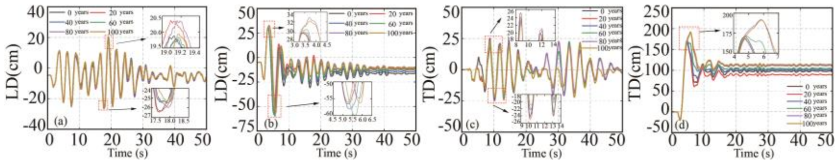

Figure 10. Displacement of bearing: (a) and (c) is under near-fault ground motions; (b) and (d) is under cross-fault ground motions; TD indicate transverse displacementand LD indicate longitudinal displacement

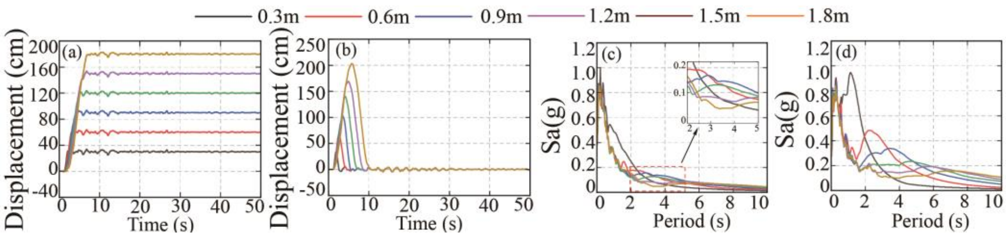

Figure 11. Seismic curve: (a) and (b) indicate time-history curves of theFP and FN fault-crossing ground motions for the six levels of PGRD; (c) and (d) indicate the related spectral acceleration (Sa)

(0-40 years), the peak bearing displacement increases as the structural stiffness reduces. However, as corrosion becomes severe (80-100 years), the peak dynamic displacement exhibits a descending trend. Severely corroded piers, having reduced flexural capacity, enter the plastic range earlier and undergo extensive inelastic deformation.

5. Analysis of fault-crossing seismic parameter responses

To investigate the mechanisms by which fault-crossing parameters govern the structural response, this approach systematically explores how variations in PGRD, FCA, and ground-motion frequency content affect the seismic response of corroded CRFBs.

5.1 Effect of PGRD

In this study, the PGRD was varied across six cases: 0.3 m, 0.6 m, 0.9 m, 1.2 m, 1.5 m, and 1.8 m. The corresponding FP and FN ground motion time histories and their acceleration response spectra for these six PGRD levels are presented in Fig. 11. Fig. 12 illustrates the responses of the main girder, piers, and bearings for different PGRD levels and corrosion durations. For any given corrosion level, the overall bridge response exhibits a distinct nonlinear trend: it first increases with PGRD, peaks at about 0.6 m, and then decreases. This behavior arises primarily because the pierstransition from linear-elastic to nonlinear-plastic response as PGRD grows. It should be noted that the observed peak at approximately 0.6 m is intrinsically tied to the structural configuration of the prototype bridge and the specific suite of ground motions employed in this study. Rather than representing a universal critical threshold, generalizing the exact magnitude of this plateau across other bridge typologies, varying stiffness distributions, or diverse seismic inputs would necessitate further robust statistical validation. The formation of plastic hinges at the pier bases limits the inertial forces transmitted to the superstructure, which corresponds to the plateau and decline seen in the acceleration response spectra. Moreover, a critical interaction effect is observed: for a fixed PGRD, the amplification of seismic response due to corrosion is far more pronounced when the PGRD-induced demands are already large. Conversely, when the base demand from PGRD is small, the impact of corrosion is negligible. Under extreme PGRD conditions, the surrounding soil medium inevitably enters a state of extensive plasticity or large-scale sliding. Although the adopted p-y and t-z springs cannot explicitly simulate the continuous plastic flow or micro-level tearing of the soil medium, they effectively capture the post-yield force-limiting saturation effect and the pile-soil separation phenomenon. Nonetheless, the structural responses derived under such massive ground distortions should still be interpreted with caution.

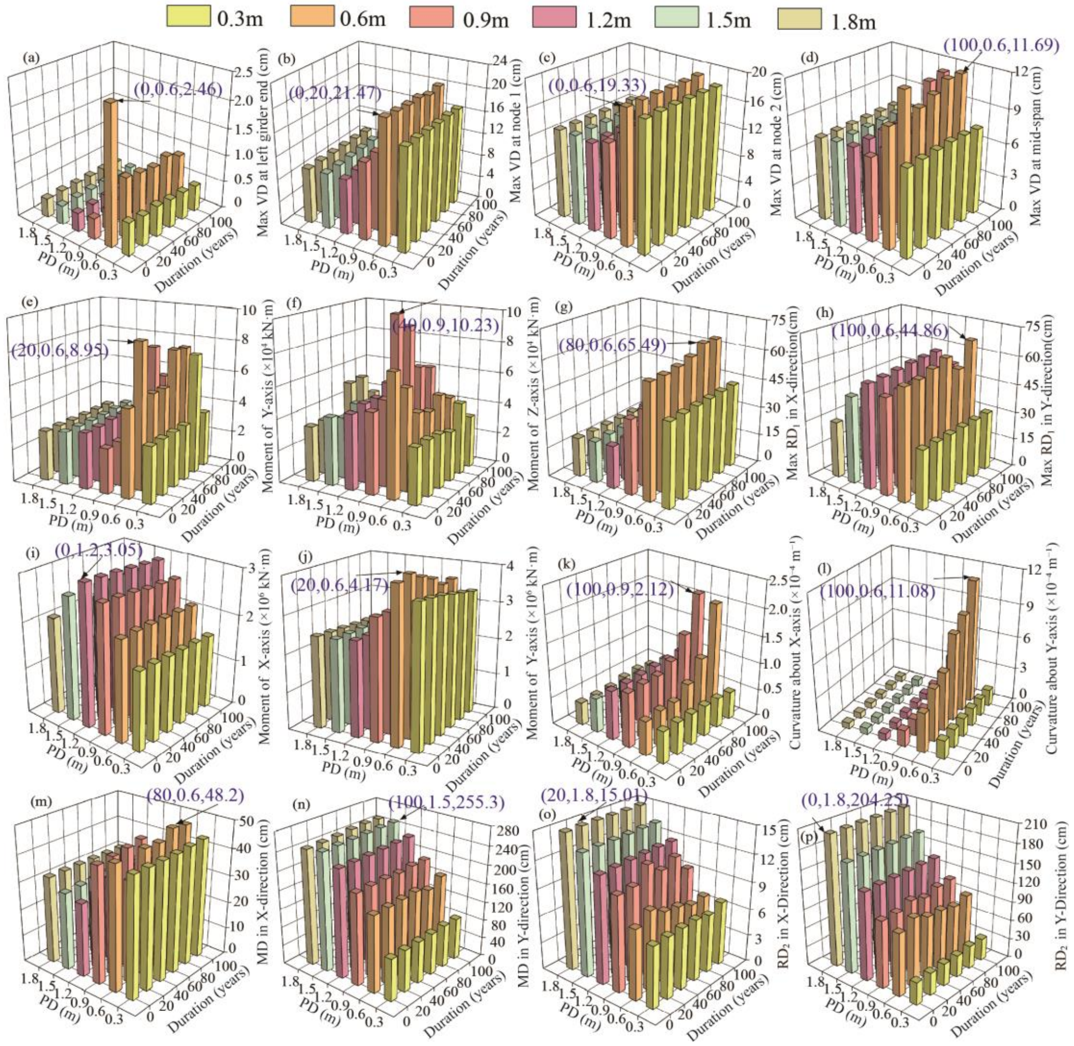

Figure 12. Seismic responses of corroded CRFBs under varying levels of PGRD: (a)-(d) maximum vertical displacements (VD) at specific locations along the main girder; (e)-(f) maximum moments of the main girder about the Y and Z axes; (g)-(h) maximum relative displacements (RD_1) at the pier tops; (i)-(l) moments and curvatures at the pier bases; and (m)-(p) maximum displacements (MD) and residual displacements (RD_2) of the bearings

5.2 Effect of FCA

To evaluate the effect of the FCA on the seismic response of corroded CRFBs, assuming a symmetrical bridge alignment with respect to the fault, the baseline ground motion (PGRD = 1.8 m) was decomposed into GMh and GMz components at the bridge supports using the vector decomposition principle, as formulated in Eq. (6). A total of eleven FCA cases were analyzed, with the angle systematically varied from 15° to 165° in 15° increments. A schematic of the bridge fault-crossing configuration, along with the resulting GMh and GMz ground motions applied at pier 4 for the different angles, is illustrated in Fig. 13.

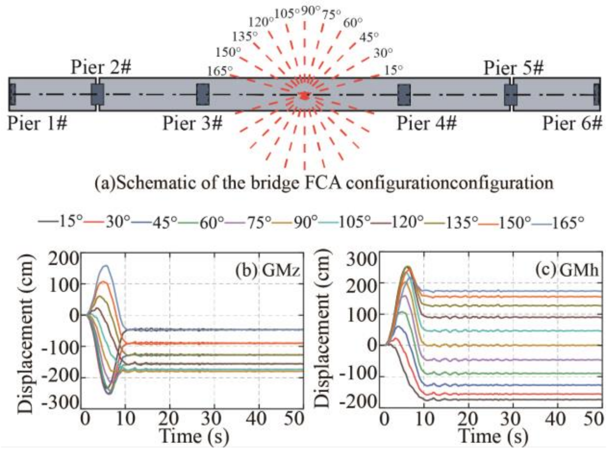

Figure 13. FCA configuration and corresponding input ground motions

$$\begin{pmatrix} GM_z \\ GM_h \end{pmatrix} = \begin{bmatrix} \sin\alpha & \cos\alpha \\ -\cos\alpha & \sin\alpha \end{bmatrix} \begin{bmatrix} F_N \\ F_P \end{bmatrix} \tag{6}$$

The distribution of structural responses, depicted in Fig. 14, indicates that the FCA has a pronounced influence on the seismic performance of CRFBs. Overall, the response magnitudes follow a distinct 'M'-shaped distribution as the FCA varies, confirming that 90° emerges as the most favorable FCA for this specific structural configuration. Changes in the FCA alter the seismic input, while corrosion modifies the structure's dynamic characteristics. The coupling of these effects results in a highly complex and uncertain response for this specific displacement at girder end [54]. Notably, the base of pier curvature can be amplified by three orders of magnitude as the FCA deviates from 90°. This is because the fault displacement imposes a large quasi-static component in the bridge's longitudinal direction. At a 90° crossing, the PGRD from the FP motion is resisted primarily by a small transverse rotation of the stiff superstructure. However, at acute or obtuse angles, this displacement resolves into a substantial longitudinal component, which imposes a large quasi-static deformation upon the highly flexible longitudinal system. This confirms that 90° serves as the most advantageous FCA for minimizing the most critical structural demands within the context of the examined bridge. Furthermore, the influence of corrosion becomes most pronounced at angles that deviate significantly from the 90° perpendicular, corrosion not only amplifies the magnitude of key responses, but also increases the overall scatter and variability in the results. It is imperative to note that this "M-shaped" sensitivity and the favorability of the 90° crossing angle are heavily contingent upon the specific bridge configuration and the load decomposition scheme employed in this study. Its general applicability to other bridge typologies has not yet been fully established and warrants systematic verification in future multi-parameter investigations.

5.3 Effect of frequency content

A comparative analysis was performed to decouple the influences of the two distinct physical mechanisms within fault-crossing ground motions [55, 56]. Three ground motions with distinct frequency content (low-frequency only, high-frequency only, and broadband), all derived from the

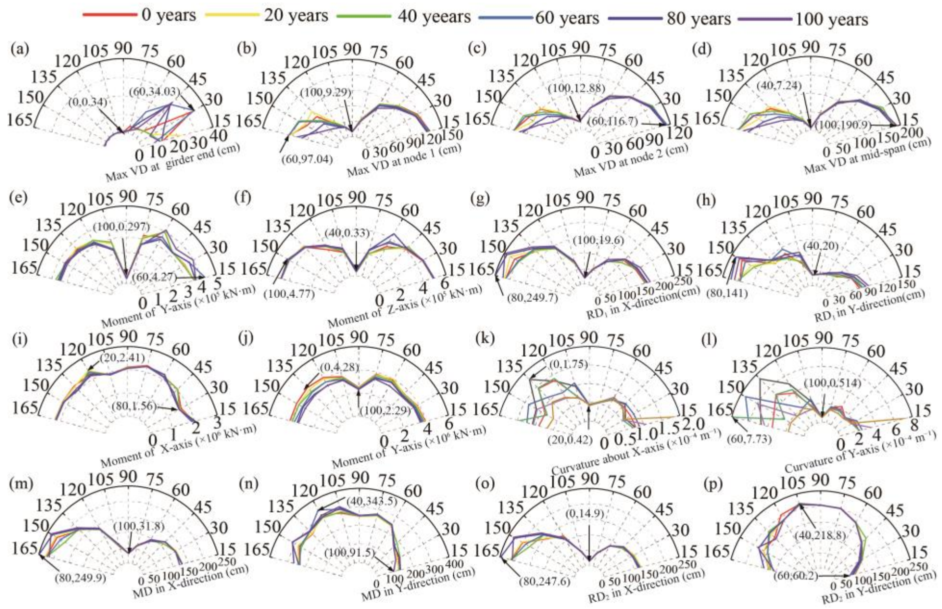

Figure 14. Parametric sensitivity of the seismic responses of corroded CRFBs to different FCA: (a)-(d) maximum vertical displacements (VD) at specific locations along the main girder; (e)-(f) maximum moments of the main girder about the Y and Z axes; (g)-(h) maximum relative displacements (RD_1) at the pier tops; (i)-(l) moments and curvatures at the pier bases; and (m)-(p) maximum displacements (MD) and residual displacements (RD_2) of the bearings

baseline case (FCA = 90°, PGRD = 1.8 m), were used for this purpose. Fig. 15 illustrates the responses of CRFBs under the aforementioned conditions. A clear frequency decoupling phenomenon was observed. Regarding the main girder vertical displacement at node 2, the HF component induces a peak response of 13.2 cm, which almost perfectly aligns with the total broadband response of 13.0 cm, demonstrating its absolute dominance. In stark contrast, the residual bearing displacement in the transverse direction is almost exclusively driven by the LF pulse. The LF component produces a permanent offset of 205 cm, essentially 100% of the 204 cm broadband response, whereas the HF component provides a negligible contribution of merely 0.22 cm. Furthermore, the pier base curvature exhibits a directionally coupled demand: the HF transient waves dictate the dynamic curvature about the Y-axis (reaching 5.78×10^{-4} m^{-1} and the broadband response of 5.25×10^{-4} m^{-1}), while the LF component governs the massive quasi-static drift curvature about the X-axis (producing 4.95×10^{-4} m^{-1} and the broadband response of 4.21×10^{-4} m^{-1}). For the main girder, the vertical displacement and the moment about the Y-axis are predominantly governed by the high-frequency component. The transverse displacement at the top of pier, the base of pier moment and curvature about the X-axis are controlled by the low-frequency component. In contrast, the longitudinal displacement at the top and the base moment and curvature about the Y-axis are dominated by the high-frequency component. For the bearings, the peak transverse displacement and the residual displacements in both directions are quasi-statically controlled by the PGRD and velocity pulse contained within the low-frequency component. This occurs because the permanent transverse displacement forces the entire superstructure to rotate, inducing a transverse displacement at the girder ends that significantly exceed the displacement at the top of the underlying piers. The bearing must accommodate this

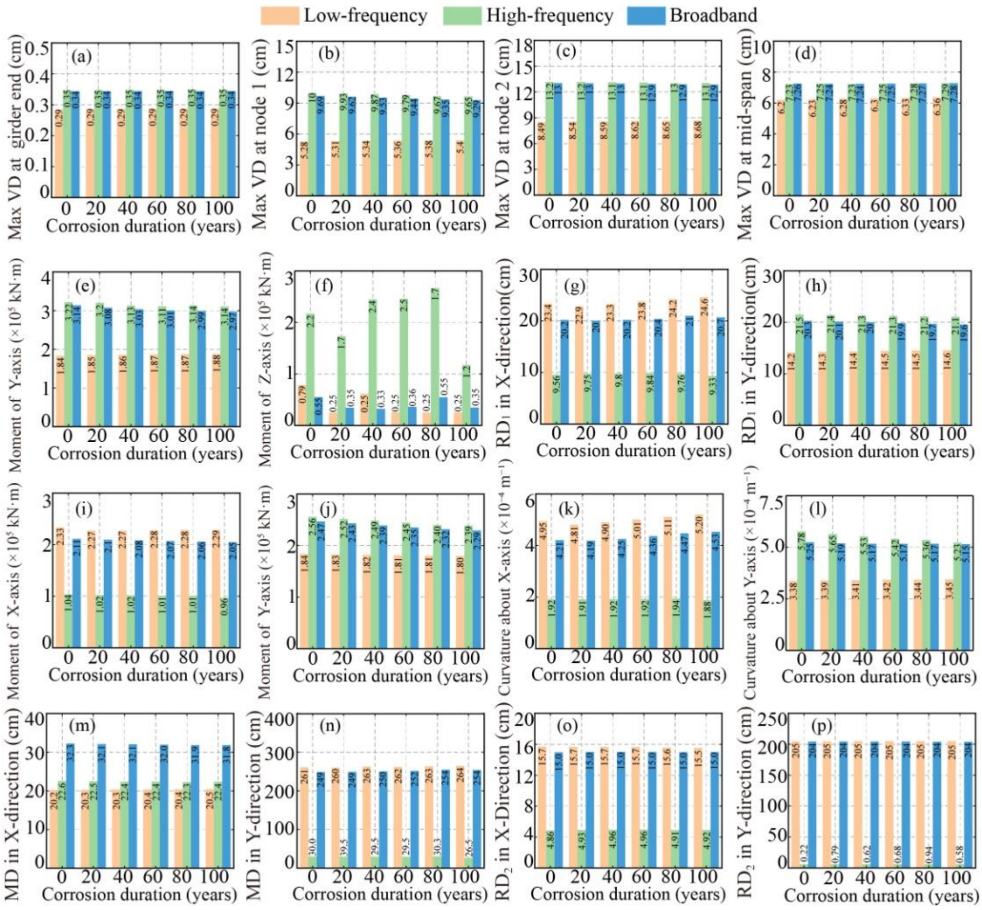

Figure 15. Decoupled effects of distinct frequency contents on the seismic responses of corroded CRFBs: (a)-(d) maximum vertical displacements (VD) at specific locations along the main girder; (e)-(f) maximum moments of the main girder about the Y and Z axes; (g)-(h) maximum relative displacements (RD_1) at the pier tops; (i)-(l) moments and curvatures at the pier bases; and (m)-(p) maximum displacements (MD) and residual displacements (RD_2) of the bearings

large differential movement. Interestingly, the superposition of the high-frequency component was found to reduce the peak transverse bearing displacement compared to the low-frequency only case. The overall structural response generally increases with the duration of corrosion.

6. Conclusions

This study investigated a representative CRFBs crossing a fault to systematically explore the differences in seismic response between near-fault and fault-crossing ground motions in a corrosive environment. Furthermore, it conducted an in-depth analysis of the mechanisms by which key parameters, such as PGRD, FCA, and ground motion frequency content govern the structural response. The following theoretical and practical insights are drawn:

- The interaction of fault-crossing excitations and material degradation shifts the seismic response from dynamic amplification to a quasi-static forced displacement mode. This coupling exacerbates structural demands, increasing pier-top displacements by up to 11.5 cm, which necessitates displacement-based compatibility checks in seismic design.

- Corrosion causes significant incremental damage that further erodes the structural safety margin beyond the baseline fault-crossing seismic demands. This material degradation triggers a critical shift in the failure pattern: from global ductile deformation to localized plastic failure within the hinge zones.
- Structural responses exhibit a nonlinear dependence on PGRD, typically reaching an observed peak plateau at 0.6 m. This phenomenon is attributed to the saturation of inertial force transmission caused by the premature yielding of severely corroded piers.
- The FCA is the dominant determinant of structural survivability. Vector decomposition reveals a distinct 'M-shaped' sensitivity, where deviation from the optimal 90° orthogonal crossing can amplify pier base curvature by up to three orders of magnitude due to longitudinal locking effects. Strictly avoiding unfavorable oblique crossing angles during route selection is imperative.
- LF velocity pulses dictate the global kinematic drifts and permanent offsets, while HF transients dominate the local cyclic damage accumulation in the superstructure. Effective resilience enhancement requires a dual-strategy approach: providing ductility for low-frequency drifts and localized reinforcement for high-frequency stress resistance.

Acknowledgements

The research for this paper was supported partially by Sichuan Science and Technology Program (No. 2026YFHZ0008), National Science Foundation of China (No. 52178169, No. U21A20154, and No. 2021YFB1600300) and the Scientific Research and Development Project of China Railway Group Limited (2022-Special-01). The authors would like to express their sincere gratitude to all the sponsors for the financial support.

References

1. Tong, L., Wang, D., Zou, Y., Shi, F., Sun, Z. (2024). Seismic performance and damage control of large-span prestressed concrete rigid-frame bridges with high piers crossing strike-slip faults. Soil Dynamics and Earthquake Engineering, 177, 108412. https://doi.org/10.1016/j.soildyn.2023.108412.
2. Jia, H., Cheng, W., Kang, W., Zhai, Y., Zheng, S., Hui, Y. (2024). BPNN-predicted fault permanent dislocation and seismic response analyses of long-span suspension bridges crossing dip-slip faults. Soil Dynamics and Earthquake Engineering, 182, 108712. https://doi.org/10.1016/j.soildyn.2024.108712.
3. Yang, S., Mavroeidis, G.P. (2018). Bridges crossing fault rupture zones: A review. Soil Dynamics and Earthquake Engineering, 113, 545-571. https://doi.org/10.1016/j.soildyn.2018.03.027.
4. Yang, S., Mavroeidis, G.P., Ucak, A. (2020). Analysis of bridge structures crossing strike-slip fault rupture zones: A simple method for generating across-fault seismic ground motions. Earthquake Engineering & Structural Dynamics, 49, 1281-1307. https://doi.org/10.1002/eqe.3290.
5. Garini, E., Gazetas, G., Anastasopoulos, I. (2017). Evidence of significant forward rupture directivity aggravated by soil response in an Mw6 earthquake and the effects on monuments. Earthquake Engineering & Structural Dynamics, 46, 2103-2120. https://doi.org/10.1002/eqe.2895.
6. Fadaee, M., Hashemi, K., Farzaneganpour, F., Anastasopoulos, I., Gazetas, G. (2020). 3–storey building subjected to reverse faulting: Analysis and experiments. Soil Dynamics and Earthquake Engineering,

138, 106297. https://doi.org/10.1016/j.soildyn.2020.106297.
7. Gao, Q.H., Monti, G., Chang, Z.W., Wang, R., Li, Z. (2025). A novel approach for classifying acceleration-pulses and non-acceleration-pulses without any filtering techniques. Journal of Earthquake Engineering,29(11), 2262-2279. https://doi.org/10.1080/13632469.2025.2505440.
8. Liu, Z. (2025). Near-fault ground motion identification method based on local mean decomposition. Journal of Earthquake Engineering, 29(11), 2303-2360. https://doi.org/10.1080/13632469.2025.2505976.
9. Goel, R.K., Qu, B., Tures, J., Rodriguez, O. (2014). Validation of fault rupture-response spectrum analysis method for curved bridges crossing strike-slip fault rupture zones. Journal of Bridge Engineering, 19(5), 06014002. https://doi.org/10.1061/(ASCE)BE.1943-5592.0000602.
10. Yang, S., Mavroeidis, G.P., Tsopelas, P. (2022). Validation of the fault rupture-response spectrum analysis method for ordinary and seismically isolated bridges crossing strike-slip fault rupture zones. Engineering Structures, 273, 115026. https://doi.org/10.1016/j.engstruct.2022.115026.
11. Jia, H., Wu, W., Xu, L., Zhou, Y., Zheng, S., Zhao, C. (2024). Numerical simulation and damaged analysis of a simply-supported beam bridge crossing potential active fault. Engineering Structures, 301, 117283. https://doi.org/10.1016/j.engstruct.2023.117283.
12. Zhang, F., Li, S., Wang, J., Zhang, J. (2020). Effects of fault rupture on seismic responses of fault-crossing simply-supported highway bridges. Engineering Structures, 206, 110104. https://doi.org/10.1016/j.engstruct.2019.110104.
13. Park, S.W., Ghasemi, H., Shen, J., Somerville, P.G., Yen, W.P., Yashinsky, M. (2004). Simulation of the seismic performance of the Bolu Viaduct subjected to near-fault ground motions. Earthquake Engineering & Structural Dynamics, 33, 1249-1270. https://doi.org/10.1002/eqe.395.
14. Dey, A., Sil, A. (2021). Advanced corrosion-rate model for comprehensive seismic fragility assessment of chloride affected RC bridges located in the coastal region of India. Structures, 34, 947-963. https://doi.org/10.1016/j. istruc.2021.08.045.
15. Afsar Dizaj, E., Salami, M.R., Kashani, M.M. (2023). Seismic vulnerability analysis of irregular multi-span concrete bridges with different corrosion damage scenarios. Soil Dynamics and Earthquake Engineering, 165, 107678. https://doi.org/10.1016/j.soildyn.2022.107678.
16. Ma, H., Yang, Y., He, Z., Zhang, Y., Ji, F. (2019). Experimental study on mechanical properties of steel under extreme cyclic loading considering pitting damage. Ocean Engineering, 186, 106091. https://doi.org/10.1016/j. oceaneng.2019.05.073.
17. Xie, H., Yu, N., Qin, M., Zhang, Q., Kang, Y. (2025). Coupled evolution analysis of pitting behavior and corrosion-induced stress of X80 steel in the marine environment. Ocean Engineering, 334, 121547. https://doi.org/10.1016/j.oceaneng.2025.121547.
18. Wei, Y., Jiang, C., Zeng, F., Guo, S., Zhang, Y., Cheng, B. (2025). Time-variant non-probabilistic ellipsoidal reliability analysis of offshore monopiles under lateral loads considering non-uniform corrosion effects. Ocean Engineering, 341, 122617. https://doi.org/10.1016/j.oceaneng.2025.122617.
19. Su, J., Li, J., Wu, D., Lu, G., Wang, L., Ma, J., Li, Z.X. (2025). Lifetime seismic damage evolution and resilience assessment of offshore bridges under height-varying corrosion and scour. Ocean Engineering, 326, 120883. https://doi.org/10.1016/j.oceaneng.2025.120883.
20. Lin, Y., Zong, Z.H., Tian, S.Z., Lin, J. (2018). A new baseline correction method for near-fault strong-motion records based on the target final displacement. Soil Dynamics and Earthquake Engineering, 114, 27–37. https://doi.org/10.1016/j. soildyn.2018.06.036.
21. Lin, Y., Zong, Z., Lin, J., Li, Y., Chen, Y. (2021). Across-fault ground motions and their effects on some bridges in the 1999 Chi-Chi earthquake. Advances in Bridge Engineering, 2, 8. https://doi.org/10.1186/s43251-020-00028-1.
22. Hu, S., Wang, Z.Y., Guo, Y., Xiao, G. (2021). Life-cycle seismic fragility assessment of existing RC bridges subject to chloride-induced corrosion in marine environment. Advances in Civil Engineering, 2021, 9640521. https://doi.org/10.1155/2021/9640521.
23. Zeng, C., Jiang, H., Bai, X.Y., Song, G.S. (2023). Study on the multi-criteria seismic mitigation optimization of a single pylon cable-stayed bridge across strike-slip fault rupture zones. Engineering Structures, 275, 115228. https://doi.org/10.1016/j.engstruct.2022.115228.

24. Jia, H., Chen, S., Guo, D., Zheng, S., Zhao, C. (2024). Track-bridge deformation relation and interaction of long-span railway suspension bridges subject to strike-slip faulting. Engineering Structures, 300, 117216. https://doi.org/10.1016/j.engstruct.2023.117216.
25. Herrera, D., Tolentino, D. (2023). Fragility assessment of RC bridges exposed to seismic loads and corrosion over time. Materials, 16(3), 1100. https://doi.org/10.3390/ma16031100.
26. Ni Choine, M., Kashani, M.M., Lowes, L.N. (2016). Nonlinear dynamic analysis and seismic fragility assessment of a corrosion damaged integral bridge. International Journal of Structural Integrity, 7(2), 227-239. https://doi.org/10.1108/IJSI-09-2014-0045.
27. Cui, F., Zhang, H., Ghosn, M., Xu, Y. (2018). Seismic fragility analysis of deteriorating RC bridge substructures subject to marine chloride-induced corrosion. Engineering Structures, 155, 61-72. https://doi.org/10.1016/j. engstruct. 2017.10.067.
28. Xu, J.G., Cai, Z.K., Feng, D.C. (2021). Life-cycle seismic performance assessment of aging RC bridges considering multi-failure modes of bridge columns. Engineering Structures, 244, 112818. https://doi.org/10.1016/j.engstruct.2021.112818.
29. Li, C., Hao, H., Li, H., Bi, K. (2016). Seismic fragility analysis of reinforced concrete bridges with chloride induced corrosion subjected to spatially varying ground motions. International Journal of Structural Stability and Dynamics, 16(5), 1550010. https://doi.org/10.1142/S0219455415500108.
30. De Domenico, D., Messina, D., Recupero, A. (2023). Seismic vulnerability assessment of reinforced concrete bridge piers with corroded bars. Structural Concrete, 24(1), 56-83. https://doi.org/10.1002/suco.202200378.
31. Zaghian, S., Martín-Perez, B., Almansour, H. (2023). Finite element modelling of bridge piers subjected to eccentric load combined with reinforcement corrosion. Engineering Structures, 283, 115822. https://doi.org/10.1016/j.engstruct.2023.115822.
32. Wang, H., Li, A. (2023). Effects of mixed corrosion damage on constitutive relation and ductile fracture behavior of butt-welded joints under cyclic loading. Structures, 55, 2341-2357. https://doi.org/10.1016/j.istruc.2023.07.028.
33. Du, Y.G., Clark, L.A., Chan, A.H.C. (2005). Residual capacity of corroded reinforcing bars. Magazine of Concrete Research, 57(3), 135-147. https://doi.org/10.1680/macr.2005.57.3.135.
34. Kashani, M.M., Crewe, A.J., Alexander, N.A. (2017). Structural capacity assessment of corroded RC bridge piers. Proceedings of the Institution of Civil Engineers-Bridge Engineering, 170(1), 28-41. https://doi.org/10.1680/jbren.15.00023.
35. Lin, M., Dai, F., Li, J. (2017). Nonlinear stress–strain behavior of corrosion-damaged reinforcing bars including inelastic buckling. Advanced Engineering Research, 136, 288-291. https://doi.org/10.2991/icadme-17.2017.56.
36. Zhang, Q., Kang, X.Q., Zhu, J.C., Hu, D.K., Zhao, H.T., Gong, J.X. (2025). Study on hysteretic model of flexure-shear critical reinforced concrete columns including the non-linear degradation effects of cyclic loading. Structures, 73, 108350. https://doi.org/10.1016/j.istruc.2025.108350.
37. Zhang, Q., Guo, X., Zhao, H., Hu, D., Gu, X., Li, R. (2025). A probabilistic stress-strain relationship model for steel bars including the non-uniform corrosion effects in chloride environments. Case Studies in Construction Materials, 22, e04262. https://doi.org/10.1016/j.cscm.2025.e04262.
38. Zhang, Q., Zheng, N.H., Gu, X.L., Wei, Z.Y., Zhang, Z. (2022). Study of the confinement performance and stress-strain response of RC columns with corroded stirrups. Engineering Structures, 266, 114476. https://doi.org/10.1016/j.engstruct.2022.114476.
39. Li, H., Yu, Z., Mao, J., Jiang, L. (2020). Nonlinear random seismic analysis of 3D high-speed railway track-bridge system based on Opensees. Structures, 24, 87-98. https://doi.org/10.1016/j.istruc.2020.01.003.
40. Jia, H.Y., Lan, X.L., Zheng, S.X., Li, L.P., Liu, C.Q. (2019). Assessment on required separation length between adjacent bridge segments to avoid pounding. Soil Dynamics and Earthquake Engineering, 120, 398-407. https://doi.org/10.1016/j.soildyn.2019.01.031.
41. Jia, H., Liu, Z., Xu, L., Bai, H., Bi, K., Zhang, C., Zheng, S. (2023). Dynamic response analyses of long-span cable-stayed bridges subjected to pulse-type ground motions. Soil Dynamics and Earthquake Engineering, 164, 107591. https://doi.org/10.1016/j.soildyn.2022.107591.

42. Mander, J.B., Priestley, M.J.N., Park, R. (1988). Theoretical stress-strain model for confined concrete. Journal of Structural Engineering, 114(8), 1804-1826. https://doi.org/10.1061/(ASCE)0733-9445(1988)114:8(1804).
43. Muthukumar, S., DesRoches, R. (2006). A hertz contact model with non-linear damping for pounding simulation. Earthquake Engineering & Structural Dynamics, 35, 811-828. https://doi.org/10.1002/eqe.557.
44. Li, S., Zhang, F., Wang, J.Q., Alam, M.S., Zhang, J. (2017). Seismic responses of super-span cable-stayed bridges induced by ground motions in different sites relative to fault rupture considering soil-structure interaction. Soil Dynamics and Earthquake Engineering, 101, 295-310. https://doi.org/10.1016/j.soildyn.2017.07.016.
45. Tong, L., Wang, R., Wang, D. (2021). Seismic cracking mechanism and control for pre-stressed concrete box girders of continuous rigid-frame bridges: Miaoziping bridge in Wenchuan earthquake as an example. Advances in Bridge Engineering, 2, 17. https://doi.org/10.1186/s43251-021-00040-z.
46. Tong, L., Wang, D., Sun, Z., Chen, L., Shi, F. (2023). Seismic uplift effect at end spans of long-span rigid-frame bridges subjected to near-fault and far-fault ground motions. Journal of Bridge Engineering, 28(7), 05023001. https://doi.org/10.1061/JBENF2.BEENG-6023.
47. Liu, C., Fang, D. (2021). Separation of long-period components of ground motion and its impact on seismic response of long-period diagrid structures. Soil Dynamics and Earthquake Engineering, 150, 106942. https://doi.org/10.1016/j.soildyn.2021.106942.
48. Abrahamson, N.A. (2002). Velocity pulses in near-fault ground motions. Proceedings of the UC Berkeley-CUREE Symposium in Honor of Ray Clough and Joseph Penzien, Berkeley, CA, USA.
49. Makris, N., Chang, S.P. (2000). Effect of viscous, viscoplastic and friction damping on the response of seismic isolated structures. Earthquake Engineering & Structural Dynamics, 29(1), 85-107. https://doi.org/10.1002/(SICI)1096-9845(200001)29:1<85::AID-EQE902>3.0.CO;2-N.
50. Mavroeidis, G.P., Papageorgiou, A.S. (2003). A mathematical representation of near-fault ground motions. Bulletin of The Seismological Society of America, 93(3), 1099-1131. https://doi.org/10.1785/0120020100.
51. Burks, L.S., Baker, J.W. (2016). A predictive model for fling-step in near-fault ground motions based on recordings and simulations. Soil Dynamics and Earthquake Engineering, 80, 119-126. https://doi.org/10.1016/j.soildyn.2015.10.010.
52. Xu, C., Xiang, N.L., Li, J.Z., Guan, Z.G. (2022). Influence of near-fault pulse-like motion characteristics on seismic performance of tall pier bridges with fragility analysis. Journal of Earthquake Engineering, 26(4), 2001-2022. https://doi.org/10.1080/13632469.2020.1751345.
53. Zhong, J., Wei, Y.Y., Shao, Y.H., Yang, T., Liu, X.X. (2024). An efficient method for predicting the residual displacement of UBPRC columns under near-fault ground motions. Journal of Earthquake Engineering, 28(5), 1451-1473. https://doi.org/10.1080/13632469.2023.2234500.
54. Xu, S., Liu, J., Yin, X., Xu, Q. (2025). Seismic performance analysis of concrete dams considering the coupled effects of wavelet asymmetry and incident direction under near-fault ground motions. Engineering Structures, 327, 119670. https://doi.org/10.1016/j.engstruct.2025.119670.
55. Bi, K., Hao, H. (2011). Influence of irregular topography and random soil properties on coherency loss of spatial seismic ground motions. Earthquake Engineering & Structural Dynamics, 40(9), 1045-1061. https://doi.org/10.1002/eqe.1077.
56. Konakli, K., Der Kiureghian, A. (2012). Simulation of spatially varying ground motions including incoherence, wave-passage and differential site-response effects. Earthquake Engineering & Structural Dynamics, 41(3), 495-513. https://doi.org/10.1002/eqe.1141.